Physics of Plasmas

Global gyrokinetic simulation of neoclassical ambipolar electric field and its effects on microturbulence in W7-X stellarator

Cite as: Phys. Plasmas **28**, 062309 (2021); https://doi.org/10.1063/5.0047291
Submitted: 15 February 2021 • Accepted: 02 June 2021 • Published Online: 23 June 2021

J. Y. Fu, J. H. Nicolau, P. F. Liu, et al.

Physics of Plasmas ARTICLE scitation.org/journal/php

Global gyrokinetic simulation of neoclassical ambipolar electric field and its effects on microturbulence in W7-X stellarator

Cite as: Phys. Plasmas **28**, 062309 (2021); doi: 10.1063/5.0047291
Submitted: 15 February 2021 · Accepted: 2 June 2021 ·
Published Online: 23 June 2021

J. Y. Fu,[1,2] J. H. Nicolau,[2] P. F. Liu,[2] X. S. Wei,[2] Y. Xiao,[3] and Z. Lin[2,a)]

AFFILIATIONS

[1]Fusion Simulation Center, Peking University, Beijing 100871, China
[2]Department of Physics and Astronomy, University of California, Irvine, California 92697, USA
[3]Institute for Fusion Theory and Simulation, Department of Physics, Zhejiang University, Hangzhou 310027, China

[a)]Author to whom correspondence should be addressed: zhihongl@uci.edu

ABSTRACT

Global neoclassical simulations of a model equilibrium of the W7-X stellarator find an ambipolar electric field with either an ion root or an electron root solution depending on the temperature ratio between electrons and ions. The ambipolar electric field is then used as an equilibrium field in the turbulence simulations of ion temperature gradient (ITG) instability. The shear of the ambipolar electric field has modest effects on the ITG linear instability, nonlinear saturation amplitude, and turbulent transport in the ion root case. However, in the electron root case, the ambipolar electric field significantly reduces the linear ITG growth rate, turbulence intensity, and radial correlation length, resulting in an ion heat conductivity comparable to the neoclassical transport level in the strong shear region.

I. INTRODUCTION

Stellarator[1–3] is an attractive fusion reactor concept which is designed with minimal plasma current for steady state operations to avoid disruptions. However, the 3D magnetic field in the stellarator greatly enhances the neoclassical (collisional) transport over the level in the axisymmetric tokamak. Recent optimization of the magnetic configuration in the stellarator, e.g., drift orbit optimization in the Wendelstein 7-X (W7-X),[4] significantly reduces the neoclassical transport. Turbulent transport then becomes an important issue for the plasma confinement in the stellarator. For example, anomalous transport dominates the particle and heat transport in the outer region of the W7-X stellarator.[5] Density fluctuations measured by the phase-contrast imaging (PCI) in the W7-X exhibit characteristics of the microturbulence, such as ion temperature gradient (ITG) turbulence.[6] Therefore, we need to improve our understanding of the properties of the microturbulence in the current experiments and in the design of future stellarators.

Even in the optimized stellarator, neoclassical transport could have significant effects on the turbulent transport. The neoclassical particle fluxes in the stellarator are intrinsically nonambipolar due to the 3D magnetic field, which leads to the formation of an ambipolar radial electric field with two possible solutions of an ion root or an electron root, depending on the temperature ratio between electrons and ions.[7] The shear of this electric field[8] could suppress the microturbulence and possibly provide a bifurcation mechanism to improved plasma confinement,[9] as observed experimentally in the W7-AS,[10] CHS,[11] and LHD[12] stellarators. The effects of the electric field shear on the ITG instability in the W7-X and LHD have been studied in linear simulations by a global gyrokinetic code EUTERPE[13] using a model electric field as a solution for the ion root. The effects of a constant electric field (i.e., no shear) on nonlinear turbulent transport in W7-X have been studied by a gyrokinetic code GENE.[14] While it is expected that a strong electric field could suppress the microturbulence,[15] an outstanding issue is whether the self-consistent neoclassical ambipolar electric field is strong enough to suppress the microturbulence in the stellarator.

Gyrokinetic simulation is a powerful tool for studying neoclassical and turbulent transport in the stellarator. Most of the previous nonlinear simulations of microturbulence in the stellarator are local flux-tube simulations,[16–18] which have provided useful insights on turbulent transport in the stellarator. The flux-tube simulation[19] assumes an axisymmetric equilibrium (i.e., every magnetic field line is equivalent), a finite magnetic shear (i.e., out-going boundary condition in the magnetic field line direction), and a radially translational symmetry

(i.e., high-n ballooning mode).[20] Recently, global nonlinear simulations of the microturbulence in the stellarator have been carried out using adiabatic electrons by the gyrokinetic codes GTC,[21] XGC-S,[22] and GENE.[23,24] Global simulation is necessary to incorporate important effects of the 3D magnetic geometry on the neoclassical and turbulent transport, such as the secular radial motion of the helically trapped particles, the localization of drift wave eigenmodes to discrete magnetic fieldlines (i.e., linear coupling of multiple-n toroidal harmonics), the effects of equilibrium sheared flows, the radial variations of turbulence intensity (e.g., turbulence spreading from linear unstable region to stable region), and the linear coupling between zonal flows and low-n harmonics of the microturbulence.[21]

In this paper, we report the first global nonlinear simulation of the microturbulence in the stellarator with the neoclassical ambipolar electric field self-consistently calculated using the GTC. Neoclassical simulation has previously been developed[25] and implemented in the GTC,[26] which was subsequently used for predicting the neoclassical transport and associated ambipolar electric field in the design of a compact stellarator.[27,28] GTC has recently been applied for simulations of both microturbulence and neoclassical transport in the stellarators and tokamaks with 3D magnetic field.[21,29–32]

In this work, GTC neoclassical simulations of a W7-X model equilibrium self-consistently calculate the ambipolar radial electric field, which exhibits either an ion root (in the case of same ion and electron temperatures) or an electron root (in the case of higher electron temperature in the core), in qualitative agreement with other drift kinetic calculations. The ambipolar electric field is then used as an equilibrium field in the GTC turbulence simulations of the ion temperature gradient (ITG) instability. The shear of the ambipolar electric fields has modest effects on the linear ITG growth rate and mode structure in the ion root case, while in the electron root case, significantly reduces the linear ITG growth rate and mostly suppresses the mode amplitude in the strong shear region. Finally, global nonlinear simulations find that the ambipolar electric field has modest effects on the ITG turbulence in the ion root case, where the turbulent transport level is much larger than the neoclassical transport. However, in the electron root case, the ambipolar electric field strongly suppresses the ITG turbulence intensity and reduces the radial correlation length, leading to an ion heat conductivity comparable to the neoclassical transport level in the high shear region. The GTC simulation results qualitatively agree with the transport analysis in a W7-X experiment,[5] which shows that the neoclassical and turbulent heat flux dominates the heat transport in the high and low shear region, respectively.

The paper is organized as follows. The GTC neoclassical and turbulence simulation models for the stellarator are described in Sec. II. Simulations of neoclassical transport and self-consistent ambipolar electric field in the W7-X are presented in Sec. III. Section IV describes simulations of the effects of ambipolar electric field on the ITG turbulence and transport. Finally, conclusions and discussions are discussed in Sec. V.

II. SIMULATION MODEL AND STELLARATOR GEOMETRY

There is an important difference between neoclassical and turbulent transport concerning ambipolarity in the stellarator.[33] As demonstrated in gyrokinetic simulations, turbulent transport is automatically ambipolar due to the quasi-neutrality constraint for the microturbulence with the frequency much smaller than the plasma frequency and the wavelength much longer than the Debye length.[34] However, the neoclassical transport is, in general, not ambipolar unless the electric field assumes a particular value. The neoclassical ambipolar electric field E_r can thus be calculated from the neoclassical simulation, without the knowledge of the turbulent transport. The shear of the ambipolar electric field could then affect the microturbulence.

In this section, the simulation model for neoclassical transport and electrostatic turbulence with ambipolar electric field is described in Sec. II A, and the implementation of 3D toroidal geometry, equilibrium profiles, and other simulation settings are described in Sec. II B.

A. Neoclassical and turbulence simulation models

We begin with the gyrokinetic equation[34,35] describing toroidal plasmas in an inhomogeneous magnetic field,

$$\frac{d}{dt}f_\alpha(\boldsymbol{X},\mu,v_\parallel,t)=\left[\frac{\partial}{\partial t}+\dot{\boldsymbol{X}}\cdot\nabla+\dot{v}_\parallel\frac{\partial}{\partial v_\parallel}-C\right]f_\alpha=0, \tag{1}$$

where

$$\dot{\boldsymbol{X}}=v_\parallel\boldsymbol{b}+\boldsymbol{v}_{\boldsymbol{E}}+\boldsymbol{v}_{\boldsymbol{d}},$$
$$\dot{v}_\parallel=-\frac{1}{m_\alpha}\frac{\boldsymbol{B}^*}{B}\cdot(\mu\nabla B+Z_\alpha e\nabla\phi).$$

Here, the subscript α denotes the particle species (i for ion and e for electron), $f_\alpha(\boldsymbol{X},\mu,v_\parallel,t)$ is the gyrocenter distribution function, $\boldsymbol{X}$ is the gyrocenter position, μ is the magnetic moment, $v_\parallel$ is the parallel velocity, t is the time, C is the collision operator, $Z_\alpha e$ and m_α are the charge and mass, respectively. $\boldsymbol{B}$ is the equilibrium magnetic field, B is the magnitude of magnetic field, $\boldsymbol{B}^*=\boldsymbol{B}+\frac{Bv_\parallel}{\Omega_\alpha}\nabla\times\boldsymbol{b}$, $\Omega_\alpha=\frac{Z_\alpha eB}{cm_\alpha}$ is the Larmor frequency, c is the speed of light, and $\boldsymbol{b}=\frac{\boldsymbol{B}}{B}$. The $\boldsymbol{E}\times\boldsymbol{B}$ drift and magnetic drift are $\boldsymbol{v}_{\boldsymbol{E}}=\frac{c\boldsymbol{b}\times\nabla\phi}{B^*}$, $\boldsymbol{v}_{\boldsymbol{d}}=\boldsymbol{v}_{\boldsymbol{c}}+\boldsymbol{v}_{\boldsymbol{g}}=\frac{cm_\alpha v_\parallel^2\nabla\times\boldsymbol{b}}{Z_\alpha eB^*}+\frac{c\mu\boldsymbol{b}\times\nabla B}{Z_\alpha eB^*}$, here $B^*=\boldsymbol{b}\cdot\boldsymbol{B}^*$, $\boldsymbol{v}_{\boldsymbol{c}}$ and $\boldsymbol{v}_{\boldsymbol{g}}$ are the magnetic curvature and gradient drifts. $\phi=\langle\phi\rangle+\delta\phi+\phi_{nc}$ is the gyroaveraged total electrostatic potential, which includes zonal component $\langle\phi\rangle(\psi)$, nonzonal component $\delta\phi(\psi,\theta,\zeta)$, and neoclassical ambipolar component $\phi_{nc}(\psi)$. Here, the neoclassical ambipolar electric field is dominated by the flux surface-averaged component since plasma rotation is heavily damped by the 3D magnetic geometry of the stellarator. The $\boldsymbol{E}\times\boldsymbol{B}$ drift velocity $\boldsymbol{v}_{\boldsymbol{E}}$ can be separated into the turbulent part $\boldsymbol{v}_{\boldsymbol{E}_{turb}}=\frac{c\boldsymbol{b}\times\nabla(\langle\phi\rangle+\delta\phi)}{B^*}$ and the neoclassical part $\boldsymbol{v}_{\boldsymbol{E}_{nc}}=\frac{c\boldsymbol{b}\times\nabla\phi_{nc}}{B^*}$.

To reduce the particle noise, the perturbative δf method[36,37] is used in both the turbulence and neoclassical simulations. The distribution function $f_\alpha=f_{0\alpha}+\delta f_\alpha$ can be decomposed into the equilibrium part $f_{0\alpha}$ and the perturbed part δf_α. The propagator in Eq. (1) is also separated into the equilibrium part L_0 and the perturbed part δL. Equation (1) can then be written as $(L_0+\delta L)(f_{0\alpha}+\delta f_\alpha)=0$. The equilibrium distribution function $f_{0\alpha}$ is defined by

$$L_0 f_{0\alpha}=0. \tag{2}$$

The perturbed distribution function is dynamically calculated by

$$(L_0+\delta L)\delta f_\alpha=-\delta L f_{0\alpha}. \tag{3}$$

The propagators and equilibrium distribution function are defined differently for the neoclassical simulation model and for the turbulence simulation model.

For the neoclassical simulation with collisions, the propagators L_0 and δL are defined as

$$L_0 = \frac{\partial}{\partial t} + v_\parallel \boldsymbol{b}\cdot\nabla - \frac{1}{m_\alpha}\boldsymbol{b}\cdot\mu\nabla B\frac{\partial}{\partial v_\parallel} - C(f_{0\alpha}), \tag{4}$$

$$\delta L = (\boldsymbol{v_d} + \boldsymbol{v}_{E_{nc}})\cdot\nabla - \frac{1}{m_\alpha}\left(\frac{v_\parallel}{\Omega_\alpha}\nabla\times\boldsymbol{b}\cdot\mu\nabla B + \frac{\boldsymbol{B}^*}{B}\cdot Ze\nabla\phi_{nc}\right) \times\frac{\partial}{\partial v_\parallel} - C(\delta f_\alpha). \tag{5}$$

Both ion and electron are treated as drift kinetic particles in the neoclassical simulation.[25] Fokker–Plank collision operator, which conserves energy and momentum, is used for like-species collisions for ion and electron species, and pitch angle collision operator is used for electron–ion collisions. The equilibrium distribution function $f_{0\alpha}$ for the neoclassical simulation is a local Maxwellian,[25] which is an exact solution of Eq. (2) since the guiding center magnetic drifts are not included in the equilibrium propagator L_0 defined in Eq. (4). Combining the gyrokinetic Poisson's equation and guiding center continuity equation, the ambipolar radial electric field E_r is calculated from the equation,[38]

$$\frac{dE_\psi}{dt}\left\langle\frac{|\nabla\boldsymbol{\psi}|^2}{B^2}\right\rangle = -\frac{1}{m_i n_i c^2}\sum_\alpha Z_\alpha e\left\langle\int d^3v\,\delta f_{n\alpha}(\boldsymbol{v_d}+\boldsymbol{v}_{E_{nc}})\cdot\nabla\psi\right\rangle, \tag{6}$$

where the angle bracket $\langle\ldots\rangle$ represents the flux-surface average, the symbol $|\ldots|$ means taking the amplitude of a vector, and v is the velocity. Here we define $E_\psi \equiv -\frac{\partial\phi_{nc}}{\partial\psi}$, ψ is poloidal magnetic flux, and the relation between E_ψ and radial electric field E_r is $E_r = E_\psi|\nabla\psi|$. The complete description of this neoclassical simulation model with the E_r can be found in Ref. 29.

For the collisionless turbulence simulation, the propagators L_0 and δL are defined as

$$L_0 = \frac{\partial}{\partial t} + \left(v_\parallel\boldsymbol{b}_0 + \boldsymbol{v_d} + \boldsymbol{v}_{E_{nc}}\right)\cdot\nabla - \frac{1}{m}\frac{\boldsymbol{B}^*}{B^*}\cdot(\mu\nabla B + Ze\nabla\phi_{nc})\frac{\partial}{\partial v_\parallel}, \tag{7}$$

$$\delta L = v_{Eturb}\cdot\nabla - \frac{1}{m}\frac{\boldsymbol{B}^*}{B^*}\cdot Ze\nabla(\langle\phi\rangle + \delta\phi)\frac{\partial}{\partial v_\parallel}. \tag{8}$$

In this turbulence simulation model, we assume gyrokinetic ions and adiabatic electrons. The equilibrium distribution function $f_{0\alpha}$ for turbulence simulation is the neoclassical solution from Eqs. (1)–(6). However, an analytic form of $f_{0\alpha}$ is not generally available. Similar to most of the gyrokinetic turbulence simulations, we approximate $f_{0\alpha}$ in the right-hand side of the perturbed distribution function [Eq. (3)] as a local Maxwellian. We also assume that the equilibrium parallel flow is strongly damped in the W7-X stellarator.[33] The zonal and nonzonal components of electrostatic potentials $\langle\phi\rangle$ and $\delta\phi$ are solved using the quasi-neutrality condition, and the neoclassical component ϕ_{nc} is obtained from the neoclassical simulations and considered as a static equilibrium potential in the turbulence simulation. More complete electrostatic simulation model for the stellarator is described in Ref. 21. Here, we extend this turbulence simulation model by incorporating the neoclassical ambipolar electric field E_r as a part of the equilibrium.

In both neoclassical and turbulence simulations, the gyrocenter motion follows the canonical equations in Boozer coordinates.[39] The perturbed propagator δL [Eq. (8)] is removed on the left-hand side of the perturbed distribution function [Eq. (3)] in the linear simulation of the ITG instability, while it is kept in the nonlinear simulation of the ITG turbulence. The neoclassical ambipolar potential ϕ_{nc} is considered as part of the equilibrium for the turbulence simulation, and thus kept in both the linear and nonlinear turbulence simulations.

As the first step toward self-consistent simulation of interaction between neoclassical and turbulent transport, we perform simulations of neoclassical transport and turbulent transport separately. The neoclassical ambipolar radial electric field calculated in the neoclassical simulation is then used as part of the equilibrium for the turbulence simulation. In future work, we will perform self-consistent simulations coupling neoclassical and turbulent transport.

B. Stellarator geometry

In the current simulation of the neoclassical transport and ITG turbulence[21] in the W7-X stellarator, GTC uses nonaxisymmetric equilibrium constructed by the ideal MHD code VMEC,[40] which assumes closed magnetic surfaces. The equilibrium geometry and magnetic field are provided by VMEC as the Fourier series in both the poloidal and toroidal directions on a discrete radial mesh with equidistant in the toroidal flux. These 3D data in the left-handed straight-fieldline coordinates are then transformed[30] to the Boozer coordinates as the Fourier series in the toroidal direction on discrete grid points on the 2D poloidal plane

$$B(\psi,\theta,\zeta) = \sum_n\left[B_c(\psi,\theta,n)\cos(n\zeta) + B_s(\psi,\theta,n)\sin(n\zeta)\right], \tag{9}$$

where B_c and B_s are the coefficients of the Fourier series, n is the toroidal harmonic, (ψ,θ,ζ) are the poloidal magnetic flux, poloidal angle, and toroidal angle, respectively, which form the right-handed Boozer coordinates.[41] The equilibrium geometry in the Boozer coordinates can be transformed to the cylindrical coordinates (R,Φ,Z). Here, R and Z are Cartesian coordinates on the poloidal plane, and Φ is the toroidal angle in the cylindrical coordinates. The position in R, Z and difference between Φ and ζ are all given by the Fourier series similar to Eq. (9). The equilibrium 3D magnetic field and metric tensor are represented in the GTC by a 3D quadratic spline interpolation on an equilibrium mesh.[30] On the other hand, the fluctuating quantities, such as the electrostatic potential, are represented in a global field-aligned mesh in a general toroidal geometry,[42] which provides the maximal computational efficiency without making any geometry approximation.[21]

The magnetic geometry of the W7-X stellarator used in this work is a model equilibrium adapted from Refs. 13 and 21. The W7-X has a stellarator symmetry with a field period of $N_{fp} = 5$, which means all the equilibrium quantities have a periodicity of $2\pi/N_{fp}$ in the toroidal direction, as shown in Fig. 1(a). Therefore, we can construct the equilibrium mesh in the domain $\zeta = [0, 2\pi/N_{fp}]$, with the toroidal periodicity. This field period is used in the turbulence simulation in Sec. IV. For neoclassical transport, simulations using either one-fifth of the torus or the full torus are equivalent. For turbulent transport, there are five drift wave eigenmode families corresponding to the five field

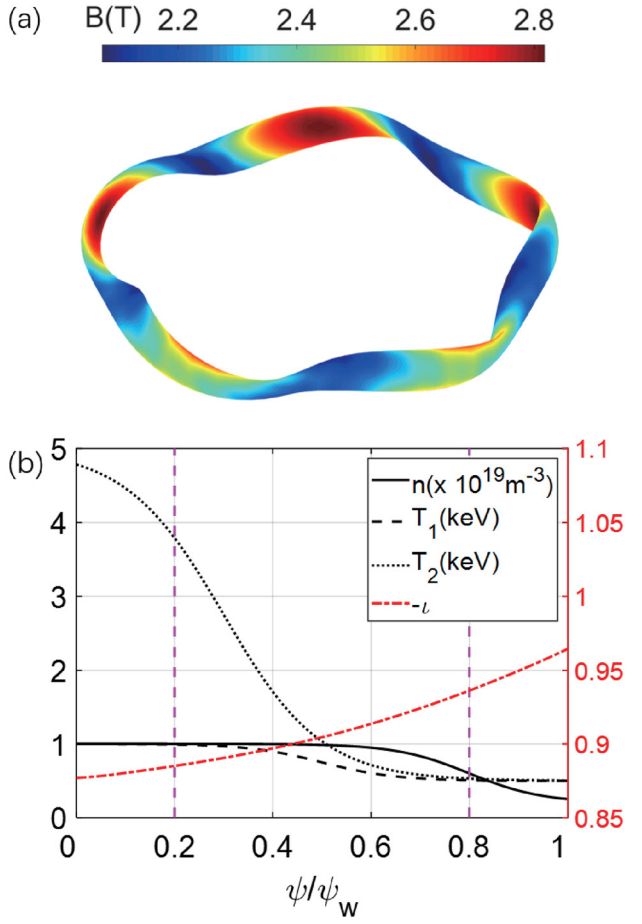

FIG. 1. (a) Real space 3D plot of magnetic field B on $\psi = 0.5\,\psi_w$ flux surface of W7-X. (b) Radial profiles of equilibrium density, temperatures, and rotational transform ι. Ion root case has $T_i = T_e = T_1$ and electron root case has $T_i = T_1$, $T_e = T_2$. The simulation domain is marked by two magenta lines: $\psi_{inner} = 0.2\,\psi_w$ and $\psi_{outer} = 0.8\,\psi_w$.

periods, and earlier GTC simulations had found similar ITG growth rates for these five eigenmodes, each coupling all toroidal n harmonics.[21]

The rotational transform ι, which represents magnetic field pitch, is plotted in Fig. 1(b). The safety factor $q = 1/\iota$, is close to the unit. The equilibrium density and temperature profiles in the neoclassical transport and ITG turbulence simulation take the form $A(\hat{\psi}) = A_0\left\{1 + A_1\left[\tanh\left((A_2 - \hat{\psi})/A_3\right) - 1\right]\right\}$, where A is the density or temperature, $\hat{\psi}$ is the poloidal magnetic flux ψ normalized with its value at the separatrix ψ_w, $\{A_0, A_1, A_2, A_3\}$ are parameters that control the details of the profile. Three profiles are shown in Fig. 1(b). For the density profile $n(\hat{\psi})$, $A_0 = 10^{19}\,\mathrm{m}^{-3}$, $\{A_1, A_2, A_3\} = \{0.4, 0.8, 0.15\}$. Two temperature profiles are used, for $T_1(\hat{\psi})$, $A_0 = 1\,\mathrm{keV}$, $\{A_1, A_2, A_3\} = \{0.25, 0.5, 0.15\}$, and for $T_2(\hat{\psi})$, $A_0 = 5\,\mathrm{keV}$, $\{A_1, A_2, A_3\} = \{0.45, 0.3, 0.2\}$.

Depending on the temperature ratio between ions and electrons, there could be two solutions for the neoclassical ambipolar electric field E_r: an electron root with $E_r > 0$, and an ion root with $E_r < 0$. We have carried out two cases with different electron temperatures. One simulation case with $T_i = T_e = T_1 \sim 1\,\mathrm{keV}$ has an ion root solution for the ambipolar electric field.[7] Another simulation case with $T_i = T_1$ and $T_e = T_2 \sim 5\,\mathrm{keV}$, which has an electron root solution due to the high electron temperature in the core, has similar temperature profiles in some W7-X experiments with electron cyclotron resonance heating (ECRH).[5,43] Note that the pressure profiles and the magnetic geometry are not fully consistent. Since all simulations presented in this manuscript are electrostatic simulations using the perturbative method (δf method), we can use various pressure profiles (e.g., ion root and electron root) for the same magnetic geometry, as is done in many gyrokinetic codes.

GTC uses three meshes: equilibrium mesh, neoclassical mesh, and turbulence mesh. The equilibrium quantities are represented on the equilibrium mesh, where the radial, poloidal, and toroidal grid numbers are, respectively, 200, 799, and 51 over one field period (i.e., one-fifth of the whole torus). In the neoclassical simulation, the momentum and energy conservation in the Fokker–Plank collision operator are enforced on a neoclassical mesh, where the radial, poloidal, and toroidal grid numbers are, respectively, 64, 64, and 32 based on the convergence studies.[25] The neoclassical ambipolar electric fields are averaged over the flux surface and thus represented on the turbulence mesh. We use both the drift kinetic ion and electron in the neoclassical simulations with realistic electron mass and ion mass. Based on the convergence studies, the particle number is 2.3×10^6 for both the ion and electron. The effective collision frequency is defined as $\nu^* = \varepsilon^{-3/2}\nu q R_0/v_{th}$, where $\varepsilon = r/R_0$ is the local inverse aspect ratio, r is the radius evaluated on the outer midplane at $\zeta = 0$, $R_0 = 5.62\,\mathrm{m}$ is the mean major radius over $\zeta = [0, 2\pi]$, ν is the physical collision frequency, and $v_{th} = \sqrt{T_{0\alpha}/m_\alpha}$ is the thermal velocity of the ion or electron. Both the ion root and electron root cases are in the long mean free path regime. For the ion root case, ν^* at $\psi = 0.5\,\psi_w$ is 0.64 for the ion, and 0.75 for the electron. For the electron root case, ν^* at $\psi = 0.5\,\psi_w$ is 0.64 for the ion, and 0.43 for the electron. Here ψ_w is the value of ψ at the separatrix. The time step size in the simulation is $\Delta t = 0.000\,25 R_0/C_s$, where $C_s = \sqrt{\frac{T_e}{m_i}}$ is the speed of the ion-acoustic wave.

In most of the linear ITG simulations, one-fifth of the W7-X torus is used with toroidal periodicity. Based on convergence studies,[21] the radial, poloidal, and parallel grid numbers are, respectively, 128, 2200, and 9 over one-fifth of the torus in the turbulence mesh for the perturbed electrostatic potentials. The only exception is the electron root case, which requires 256 radial grids for numerical convergence. The turbulence mesh is the global field-aligned mesh,[42] which allows us to use a small parallel grid number since the ITG mode has $k_\parallel \ll k_\perp$. The nine parallel grids over one-fifth of the torus correspond to about 50 grids per parallel wavelength since the ITG mode parallel wavelength is on the order of the connection length ($2\pi qR$). Without the global field-aligned mesh, the toroidal grid number would have to be about 2000 (i.e., 220 times more expensive) to achieve the same resolution. The number of particles per cell is 50, and the time step size is $\Delta t = 0.01 R_0/C_s$. The time step size convergence has been studied in earlier GTC simulations of the ITG turbulence in the same W7-X equilibrium.[21] In the nonlinear ITG simulations, the number of

particles is four times larger than the linear simulations to achieve the numerical convergence, and the time step size and the grid points are the same as the linear simulations.

The region with a strong pressure gradient, $\hat{\psi} = [0.2, 0.8]$, is chosen as the simulation domain for both the neoclassical and turbulent transport. In the buffer zone ($\hat{\psi} < 0.3$ or $\hat{\psi} > 0.7$), equilibrium density and temperature gradients are set to be zero and the perturbed electrostatic potential is smoothly suppressed to be zero at the radial boundaries. When a particle goes outside the radial boundary in the simulation, it is put back to the simulation domain and its weight is set to zero. So the particles that go outside the radial simulation domain will not affect the self-consistent electrostatic potential, but the total marker number is kept constant.

III. SIMULATION OF NEOCLASSICAL AMBIPOLAR ELECTRIC FILED IN W7-X

A. Neoclassical ambipolar electric field

In GTC neoclassical simulations solving Eqs. (1)–(6), the radial electric field is initially set to zero. Radial current is subsequently generated by the difference between ion and electron particle fluxes $\Gamma_\alpha = \langle \int d^3v\, \delta f_\alpha (\boldsymbol{v_d} + \boldsymbol{v_E}) \cdot \nabla\psi \rangle$, which induced a radial electric field E_r to maintain neutrality. Time history of the volume-averaged Γ_α in the ion and electron root cases are shown in Fig. 2(a). After about half of the ion collision time $\tau_i = 1/\nu_i$, ambipolar state is achieved with the steady state E_r in both ion and electron root cases. Even though the Γ_α has some fluctuation in the time evolution, the E_r shown in Fig. 2(b) is the time integration of Γ_α, thus it is much smoother. During the E_r evolution, the geodesic acoustic mode (GAM) oscillation is not visible, because of the large damping rate of the GAM due to the low safety factor $q = \frac{1}{\iota} \sim 1.1$ in the W7-X.[44]

Figure 2(c) shows the neoclassical ambipolar electric field E_r at the steady state in the neoclassical simulations of the ion and electron root cases. The ion root case has a relatively flat ambipolar electric field with $E_r < 0$ across the whole simulation domain. In contrast, the electron root case has a much stronger ambipolar electric field with $E_r > 0$ in the inner region, and $E_r < 0$ in the outer region, which creates a strong $\boldsymbol{E} \times \boldsymbol{B}$ flow shear around the $\hat{\psi} \sim 0.5$ flux surface. This E_r profile of the electron root agrees qualitatively with other neoclassical codes [e.g., Drift Kinetic Equation Solver (DKES)] and measurements in some W7-X ECRH experiments with high electron temperature,[5,43] with large positive Er values transitioning to negative Er values with an inflection point around $\hat{\psi} = 0.5$. Note that the equilibrium density and temperature profiles we use in the simulations are only qualitatively similar to the experimental profiles, so the agreement of the E_r profile between simulation and experiment is expected to be qualitative.

B. Neoclassical transport with self-consistent ambipolar electric field

The irreducible neoclassical transport provides a reference level for the turbulent transport in the stellarator. Neoclassical theory predicts that diffusivities are inversely proportional to collision frequency due to the helical trapped particles in the long mean free path regime of the stellarator,[45] which is different from the axisymmetric tokamak. With the neoclassical ambipolar electric field E_r, the diffusivities would

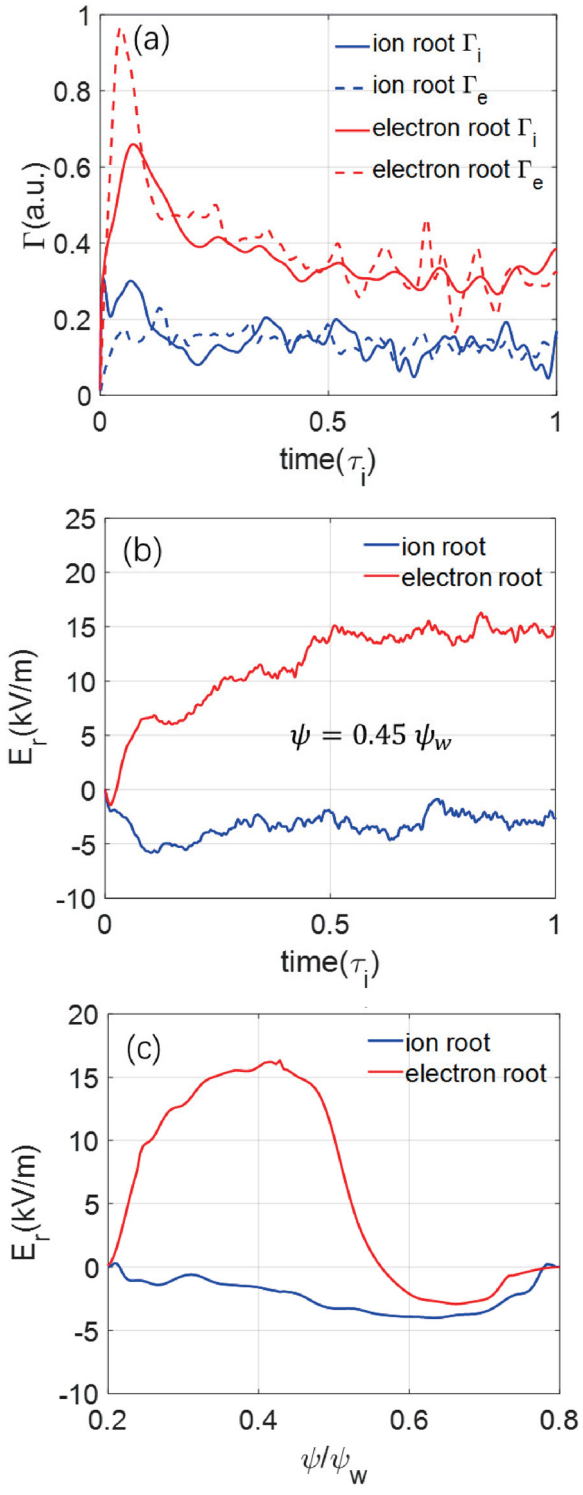

FIG. 2. Time history of volume-averaged radial particle flux Γ [panel (a)] and radial electric field E_r at $\psi = 0.45\psi_w$ [panel (b)] in neoclassical simulation of ion root case and electron root case. (c) Radial profiles of self-consistent ambipolar electric field E_r averaged over $t = [0.75, 1.0]\ \tau_i$.

decrease if E_r is large enough. In the GTC neoclassical simulations, heat conductivities are calculated as

$$\chi_\alpha = \frac{1}{\langle|\nabla\psi|^2\rangle n_{0\alpha}\frac{\partial T_{0\alpha}}{\partial\psi}}\left\langle\int d^3v\,\delta f_\alpha\left(\frac{1}{2}m_\alpha v^2-\frac{3}{2}T_{0\alpha}\right)\boldsymbol{v_d}\cdot\nabla\psi\right\rangle$$

and diffusivities as

$$D_\alpha = \frac{1}{\langle|\nabla\psi|^2\rangle\frac{\partial n_{0\alpha}}{\partial\psi}}\left\langle\int d^3v\,\delta f_\alpha\boldsymbol{v_d}\cdot\nabla\psi\right\rangle.$$

We compare the diffusivities and heat conductivities of ion (D_i, χ_i) and electron (D_e, χ_e) averaged over $t = [0.75, 1.0]\,\tau_i$, between simulations with or without solving the self-consistent ambipolar electric field E_r in Figs. 3 and 4, where the gyro-Bohm unit $D_{GB} = \chi_{GB} = \frac{v_i}{a}\rho_i^2$ are used for normalization, with $v_i = \sqrt{\frac{T_i}{m_i}}$ as thermal speed of ion, $a = 0.08$ R_0 as minor radius on the outer midplane at $\zeta = 0$, $\rho_i = v_i m_i c/eB$ as ion Larmor radius. The results in the buffer zone of

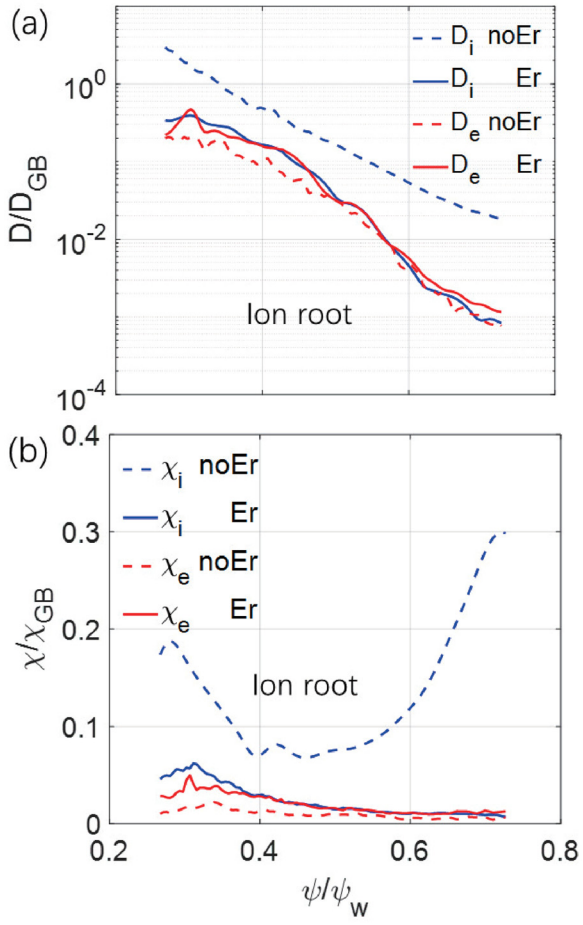

FIG. 3. Transport coefficients from neoclassical simulations of ion root case averaged over $t = [0.75, 1.0]\,\tau_i$. (a) Diffusivities D of ion and electron with or without solving self-consistent ambipolar electric field E_r. (b) Heat conductivities χ of ion and electron with or without solving E_r.

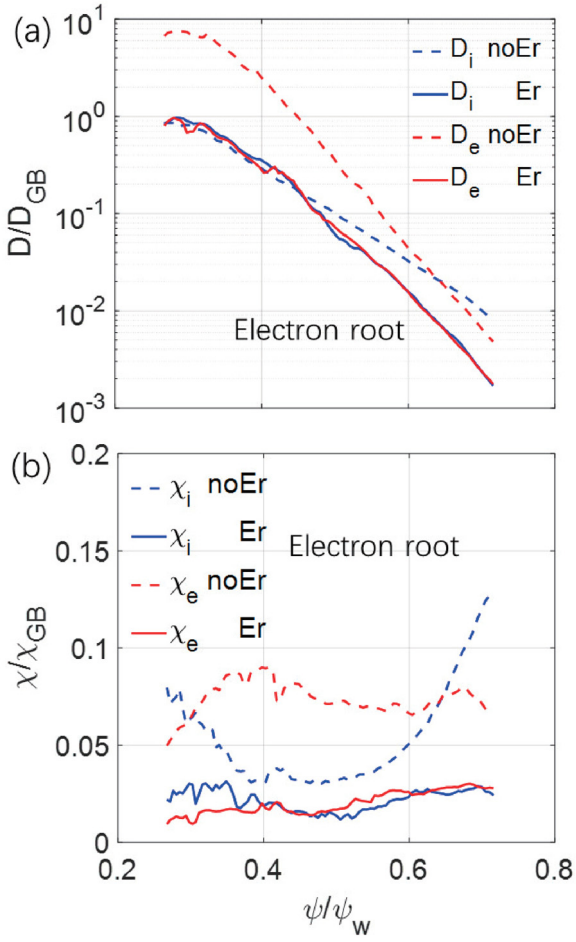

FIG. 4. Transport coefficients from neoclassical simulations of electron root case averaged over $t = [0.75, 1.0]\,\tau_i$. (a) Diffusivities D of ion and electron with or without solving self-consistent ambipolar electric field E_r. (b) Heat conductivities χ of ion and electron with or without solving E_r.

simulations near the boundary are not physical and not plotted. The diffusivities are shown in Figs. 3(a) and 4(a). In the ion root case without the E_r, the D_i is typically one order of magnitude larger than the D_e in the whole simulation domain. In the electron root case, the D_e is about three times of the D_i in the region near $\hat{\psi} \sim 0.5$, where the electrons have lower effective collision frequency than the ions. In the simulation with self-consistent ambipolar electric field E_r, both the ion root case and electron root case have $D_i \approx D_e$ in the whole simulation domain, which ensures the ambipolarity when the E_r approaches a steady state solution.

The heat conductivities are shown in Figs. 3(b) and 4(b). In the ion root case without the ambipolar electric field E_r, the χ_i is one order of magnitude larger than the χ_e in the region near $\hat{\psi} \sim 0.5$. With the E_r, the χ_e changes little, but the χ_i decreases to a level close to the χ_e. In the electron root case without the E_r, the χ_e is about two times of the χ_i. With the E_r, the χ_e decreases by a factor of four and the χ_i by a factor of two. These transport coefficients are mostly due to the helical trapped particles and agree with the neoclassical theory.[17] The

diffusivities D_α are much larger than the heat conductivities χ_α inside $\hat{\psi} = 0.6$, because the particle transport due to the helical trapped particles are mostly driven by the temperature gradient in the stellarator,[46] and the D_α can become very large due to the small density gradient in the inner region.

IV. EFFECT OF AMBIPOLAR ELECTRIC FIELD ON ITG TURBULENCE AND TRANSPORT

A. Effect of ambipolar electric field on linear ITG instability

In this subsection, we carry out linear ITG simulation solving Eqs. (1)–(3), (7), and (8), together with the ambipolar radial electric field $E_{eq} = -\frac{\partial \phi_{nc}}{\partial \psi}$ calculated in the neoclassical simulations discussed in Sec. III. The profiles of the neoclassical ambipolar electric field have different features in the ion and electron root cases. The ion root electric field is flat in mid-radius region near $\hat{\psi} \sim 0.5$ and has larger $\boldsymbol{E} \times \boldsymbol{B}$ flow shear away from the mid-radius region. On the other hand, the electron root electric field has a strong $\boldsymbol{E} \times \boldsymbol{B}$ flow shear in the mid-radius region near $\hat{\psi} \sim 0.5$. The different radial profiles of the $\boldsymbol{E} \times \boldsymbol{B}$ flow shear could have different effects on the linear ITG instability.

The radial eigenmode structures of the perturbed electric potential $\delta\phi_{rms}$ are shown in Fig. 5 for simulations with or without the neoclassical ambipolar electric field E_{eq}, together with the shearing rate ω_s of the $\boldsymbol{E} \times \boldsymbol{B}$ flow. In the ion root case with small shearing rate in the mid-radius of the simulation domain, the eigenmode structure is slightly narrower and shifts slightly inward. In the electron root case, the large shearing rate at the mid-radius of the simulation domain completely suppresses the ITG instability in the mid-radius region of $\hat{\psi} = 0.45 - 0.6$, and leaves two peaks at $\hat{\psi} = 0.42$ and $\hat{\psi} = 0.63$.

The shearing rate of $\boldsymbol{E} \times \boldsymbol{B}$ flow is defined as $\omega_s = \frac{(RB_p)^2}{B}\left|\frac{\partial^2 \phi_{nc}}{\partial \psi^2}\right|$, where R is the major radius, B_p and B are the strength of the poloidal and total magnetic field. To compare the shearing rates for the two cases, we define the mean ω_s as the average over radial mode structure $\hat{\psi} = 0.4 - 0.6$. In the ion root case, the mean $\omega_s \approx 0.2\gamma_0$ and $\gamma = 0.8\gamma_0$, where $\gamma_0 = 7.44 \times 10^4\ s^{-1}$ is the ITG growth rate without the E_{eq}. In the electron root case, the mean $\omega_s = 1.5\gamma_0$ and $\gamma = 0.27\gamma_0$, where $\gamma_0 = 9.57 \times 10^4\ s^{-1}$. Note that the linear results of the ion root case are very similar to the previous work of EUTERPE,[13] where the model ion root electric field induces about 25% reduction in the linear ITG growth rate.

The 2D spectrum of eigenmode on the diagnosed flux surface from simulations of the ITG instability in the ion root case and electron root case is shown in Fig. 6. The ratio between the dominant toroidal harmonics and poloidal harmonics is closed to the rotational transform ι of the diagnosed flux surface. On the $\hat{\psi} = 0.48$ surface in the ion root case, the dominant toroidal harmonics have a wide region from $n = 200$ to $n = 300$ due to the linear coupling between different toroidal harmonics. On the $\hat{\psi} = 0.63$ surface in the electron root case, the dominant toroidal harmonics ranges from $n = 150$ to $n = 350$. The spectra are slightly broadened by the E_{eq}, which indicates that the linear toroidal coupling could be enhanced by the E_{eq}.

B. Effects of ambipolar electric field on ITG turbulence and transport

In this subsection, we perform nonlinear simulations to study the effects of ambipolar electric field E_{eq} on the ITG turbulence in the W7-X. Both the ion root and electron root cases are studied using the equilibrium density, temperature, and neoclassical ambipolar electric field $E_{eq} = -\frac{\partial \phi_{nc}}{\partial \psi}$ same as in the linear simulations. The nonlinear terms are added to the gyrocenter motion and the zonal electric field $E_{ZF} = -\frac{\partial \langle \phi \rangle}{\partial \psi}$ generated by the turbulence is also included in the simulations, since it has been shown[21] that the zonal flows are the dominant saturation mechanism for the ITG instability in the W7-X. To prevent the temperature profile relaxation, we use an effective collision operator for energy diffusion to model a heat bath,[47] which maintains the initial ion temperature profile on a scale much longer than the turbulence correlation length.

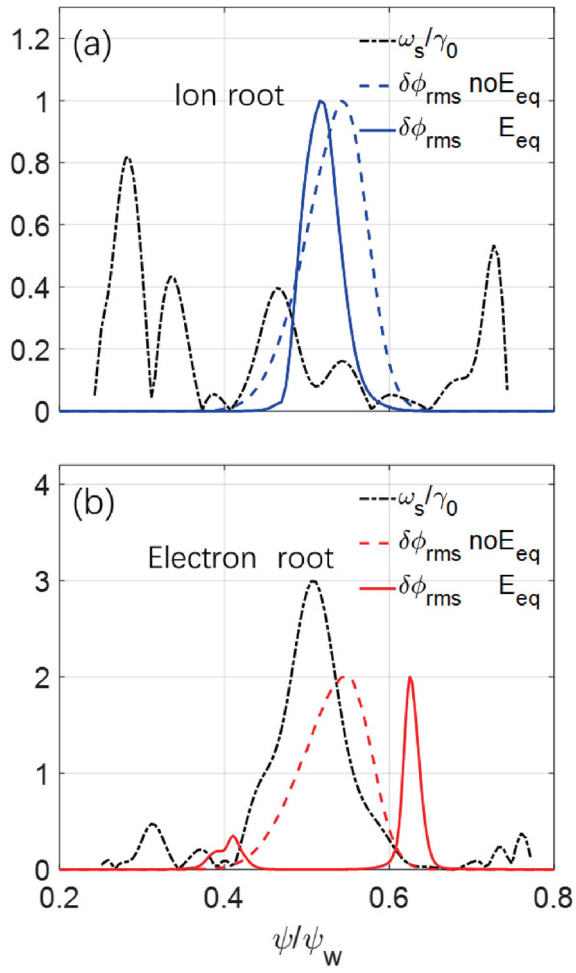

FIG. 5. Radial profiles of $\boldsymbol{E} \times \boldsymbol{B}$ flow shear ω_s (normalized with γ_0), and root mean square of $\delta\phi$ (arbitrary unit) from linear simulations of ITG instability with (solid line) or without (dashed line) ambipolar electric field E_{eq} in ion root case [panel (a)] and electron root case [panel (b)]. Root mean square of potential $\delta\phi$ is normalized by maximal value in ion root and half of the maximal value in electron root.

Figure 7 shows the history of the volume-averaged ion heat conductivity χ_i, root mean square of the nonzonal electrostatic potential $\delta\phi_{rms}$ and zonal flow $\langle\phi\rangle$ from GTC nonlinear simulations with or without the ambipolar electric field E_{eq}. The heat conductivities are

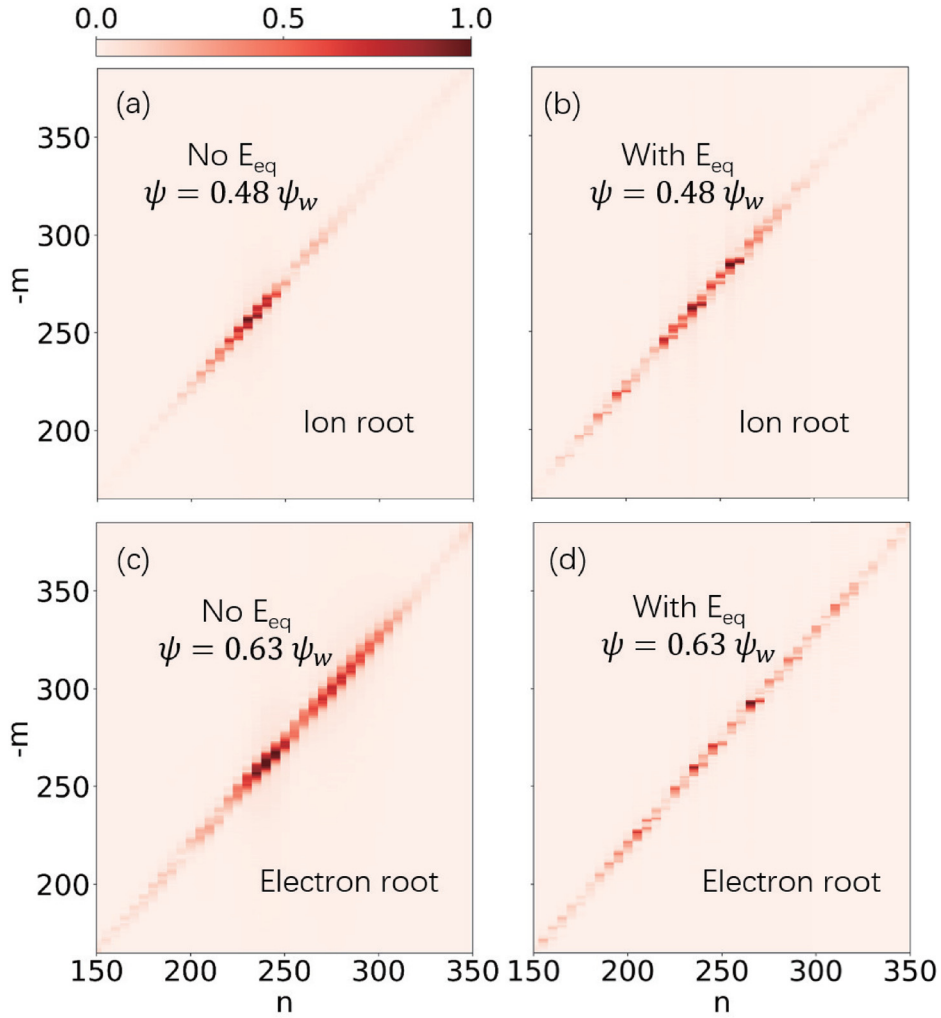

FIG. 6. Amplitude of electrostatic potential $|\delta\phi_{mn}|$ as a function of toroidal n and poloidal m harmonic from linear simulations of ITG instability with or without ambipolar electric field E_{eq} in ion root case and electron root case.

calculated as $\chi_\alpha = \frac{1}{\langle|\nabla\psi|^2\rangle n_{0\alpha}\frac{\partial T_{0\alpha}}{\partial\psi}}\left\langle\int d^3v\,\delta f_\alpha\left(\frac{1}{2}m_\alpha v^2 - \frac{3}{2}T_{0\alpha}\right)\boldsymbol{v}_{\boldsymbol{E}}\cdot\nabla\psi\right\rangle$ in the turbulence simulations. In the ion root case with the E_{eq} shown in panels (a) and (c), the saturated amplitude of the χ_i and $\delta\phi_{rms}$ are very closed to that from simulations without the E_{eq}. Therefore, the effect of the ambipolar electric field on the ITG turbulence and transport is weak in the ion root case. In contrast, the effects of the ambipolar electric field E_{eq} on the ITG turbulence and transport are very strong in the electron root case as shown in panels (b) and (d). Compared with simulations without E_{eq}, the saturated amplitudes of the χ_i and $\delta\phi_{rms}$ decrease by a factor of 3.5 and 2, respectively. In both the ion root case and the electron root case, the saturated zonal flow $\langle\phi\rangle$ amplitude in the simulation without the E_{eq} is close to that with E_{eq}, which means the zonal flow amplitude is only slightly affected by the E_{eq}. However, the shear of the zonal flow can be affected by E_{eq}, as shown in Fig. 9.

To verify that the simulation results are not affected by particle noise, all of the GTC simulations in this paper use a quasilinear theory together with the measured noise spectrum[48] to monitor the effects of the particle noise. As an example, the noise-driven heat conductivity for ion χ_i^{noise} in the ion root case without E_{eq} is shown in Fig. 7(a). During the whole simulation period, the noise-driven transport is shown to be less than 1% of the ITG-driven heat transport.

Figure 8 shows the radial profiles of the heat conductivity χ_i after ITG saturation and averaged over $t = [15, 25]R_0/C_s$ for the ion root case, and $t = [70, 80]R_0/C_s$ for the electron root case. In the ion root case, effects of the ambipolar electric field on the χ_i profiles are insignificant. The χ_i driven by the ITG turbulence is much larger than the neoclassical ion heat conductivity χ_{neo} shown in Fig. 3(b). In contrast, the shear of the ambipolar electric field in the electron root case greatly suppresses the χ_i, especially in the high shear region of the E_{eq}, which leads to two χ_i peaks at $\hat{\psi} = 0.38$ and $\hat{\psi} = 0.58$. In the high shear region near $\hat{\psi} = 0.5$, local transport is mostly driven by turbulent spreading from the low shear region. Compared to the neoclassical ion heat conductivity χ_{neo} shown in Fig. 4(b), the χ_i driven by the ITG turbulence in the low shear region is still one order of magnitude larger

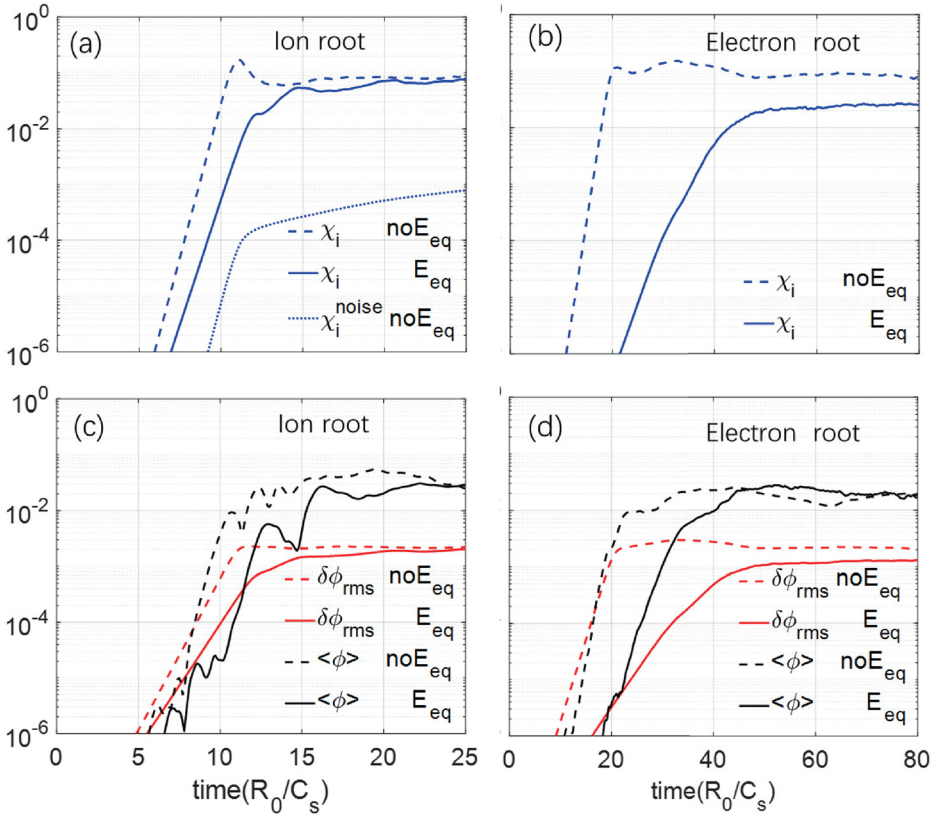

FIG. 7. History of volume-averaged ion heat conductivity χ_i (blue), nonzonal electrostatic potential $\delta\phi_{rms}$ (red) and zonal flow $\langle\phi\rangle$ from nonlinear simulations with (solid lines) or without (dashed lines) ambipolar electric field E_{eq} in ion root case [panels (a) and (c)] and electron root case [panels (b) and (d)]. χ_i is normalized with gyro-Bohm unit χ_{GB}, $\delta\phi_{rms}$ and $\langle\phi\rangle$ are normalized with T_e/e. Noise-driven heat conductivity (dotted line) for ion χ_i^{noise} in ion root case without E_{eq} is also shown in panel (a).

than the χ_{neo}, but comparable to the χ_{neo} in the high shear region near the $\hat{\psi} = 0.5$ surface.

The GTC simulation results for the turbulent transport qualitatively agree with the transport analysis based on the power balance in a W7-X experiment with ECRH,[5] which shows that the neoclassical heat flux accounts for over 50% of the total heat flux in the high shear region and that the anomalous transport dominates the heat transport in the low shear region.

Both the neoclassical ambipolar electric field and zonal flows[19] reduce the ITG turbulence intensity and transport. The radial profiles of the zonal flow electric field E_{ZF} after the ITG saturation (at $t = 25R_0/C_s$ for the ion root case and $t = 80R_0/C_s$ for the electron root case) and the neoclassical ambipolar electric field E_{eq} are shown in Fig. 9. In the ion root case shown in panel (a), the amplitude and structure of the E_{ZF} are not significantly affected by the E_{eq}, and the zonal flow shearing rate is one order of magnitude larger than that of the E_{eq}. On the other hand, in the electron root case shown in panel (b), the amplitudes of the E_{ZF} are similar between the simulations with or without the E_{eq}. However, the radial wavelength of the E_{ZF} in the simulation with the E_{eq} is much larger than that in the simulation without the E_{ZF}. Consequently, the mean shearing rate of the E_{ZF} decreases by a factor of three by the effects of the E_{eq}, and is much smaller than that of the E_{eq}, possibly due to both the reduction of the ITG turbulence intensity and the enhancement of zonal flow residual level[49] by the E_{eq}.

Figure 10 shows the perturbed nonzonal electrostatic potential $\delta\phi$ on the $\zeta = 0$ poloidal plane after ITG saturations (at $t = 25R_0/C_s$ for the ion root case and $t = 80R_0/C_s$ for the electron root case) from simulations with or without the ambipolar electric field E_{eq}. In the ion root case, the poloidal snapshot of the $\delta\phi$ without the E_{eq} is very similar to that with the E_{eq}, which indicates that the ITG turbulence is not significantly affected by the E_{eq}. In contrast, in the electron root case, the large shearing rate of the E_{eq} in the region near the $\hat{\psi} = 0.5$ flux surface strongly suppresses the local ITG turbulence, resulting in the appearance of two rings in the $\delta\phi$ poloidal snapshot [panel (d)].

The ambipolar electric field E_{eq} can also affect the radial correlation length L_r of the ITG turbulence, which is another important physical quantity measured in the experiments.[50,51] Here, we calculate the L_r in both the ion root case and the electron root case after nonlinear ITG saturation.

We define the correlation function $C_r(\Delta r) = \frac{\langle\delta\phi(r+\Delta r,\zeta)\delta\phi(r,\zeta)\rangle}{\sqrt{\langle\delta\phi^2(r+\Delta r,\zeta)\rangle\langle\delta\phi^2(r,\zeta)\rangle}}$, where r is the radial position, Δr represents the radial separation, $\langle\cdots\rangle$ represents the average over $t = [15, 25]R_0/C_s$ for the ion root case, and $t = [70, 80]R_0/C_s$ for the electron root case, i.e., about ten ion transit time, $\hat{\psi} = [0.3, 0.7]$, $\theta = 0$ and $\zeta = [0, 2/5\,\pi]$. Here we neglect the separation in the parallel direction, because of the small parallel wave vector $k_\parallel$.[21] The radial correlation length L_r is defined as the e-folding decay of the radial correlation function $C_r(L_r) = 1/e$, where e is the natural constant.

The radial correlation functions $C_r(\Delta r)$ in the ion root case and the electron root case are shown in Fig. 11. Both simulations with and without ambipolar electric field E_{eq} are compared together with the

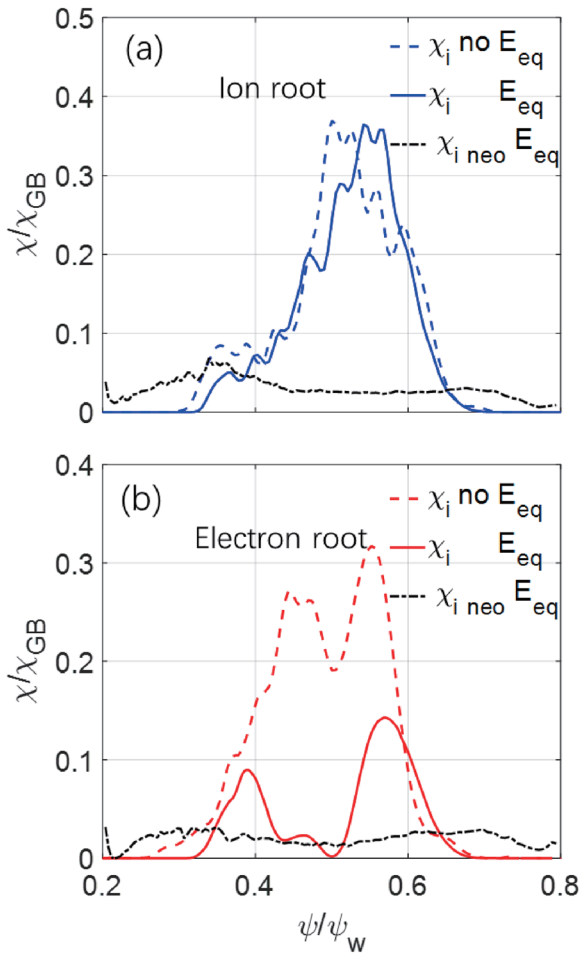

FIG. 8. Radial profiles of saturated ion heat conductivities χ_i in ITG turbulence from simulations with (solid lines) or without (dashed lines) ambipolar electric field E_{eq} in ion root case [panel (a)], and electron root case [panel (b)]. Ion heat conductivities in neoclassical simulations $\chi_{i\,neo}$(dotted–dashed line) with E_{eq} in ion root case and electron root case are also plotted for comparison.

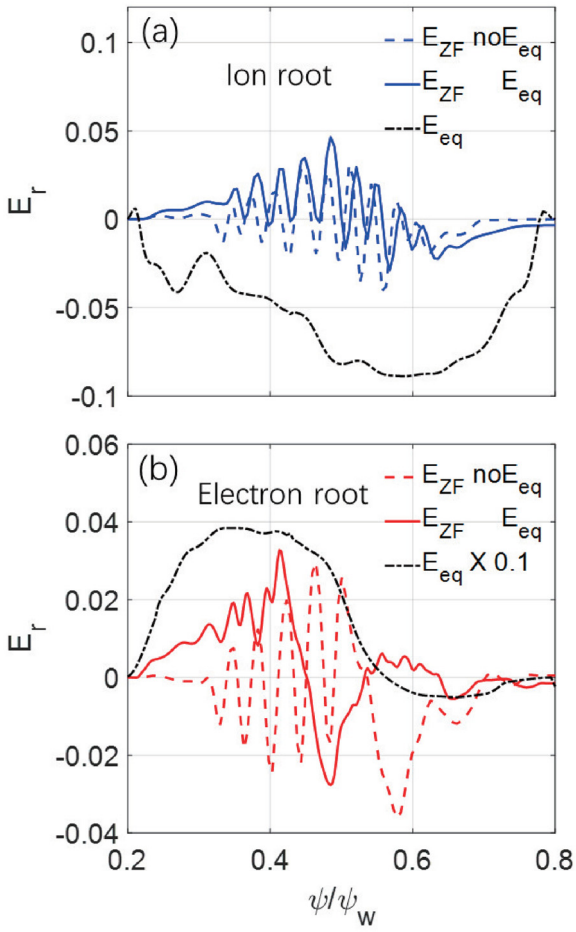

FIG. 9. Radial profiles of saturated zonal flow electric field E_{ZF} with (solid lines) or without (dashed lines) ambipolar electric field E_{eq} (dot dash lines) in ion root case [panel (a)], and electron root case [panel (b)]. $E_r = -\partial\phi/\partial\psi$ is normalized with $eB_0R_0^2/T_e$.

fitting curves of an exponential decay $\exp\left(-\frac{\Delta r}{L_r}\right)$. For the ion root case, the ambipolar electric field E_{eq} does not significantly affect the radial correlation length L_r. However, in the electron root case, the ambipolar electric field E_{eq} induces a 27% reduction of the radial correlation length L_r, from $2.2\rho_i$ to $1.6\rho_i$. The effects of the ambipolar electric field E_{eq} on the radial correlation length L_r is consistent with its effects on the ITG turbulence intensity and the ion heat conductivity.

V. DISCUSSION AND CONCLUSION

In this paper, we use GTC neoclassical simulations to self-consistently calculate the neoclassical ambipolar electric field in a model equilibrium of the W7-X stellarator for both the ion root case and electron root case, in qualitative agreement with other drift kinetic calculations. These ambipolar electric fields are then used as an equilibrium field in the GTC turbulence simulations of ITG instability. In the ion root case, the shear of the ambipolar electric field has modest effects on the linear ITG growth rate and mode structure. On the other hand, in the electron root case, the shear of the ambipolar electric field significantly reduces the linear ITG growth rate and mostly suppresses the mode structure in the high shear region. Finally, the global nonlinear simulations show that the shear ambipolar electric field has little effect on the ITG turbulence and transport in the ion root case, and the turbulent transport is much larger than the neoclassical value. In contrast, in the electron root case similar to the W7-X experiments with ECRH,[43] the effects of ambipolar electric field strongly reduce the ITG turbulence intensity and reduce the correlation length, resulting in the ion heat conductivity comparable to the neoclassical transport level in the high shear region.

The finding that the ambipolar electric field of the electron root case significantly suppresses the ITG turbulence and transport could have important implications for future stellarator reactors. In the burning plasmas, thermal electrons will be heated first by energetic fusion products (i.e., α-particle) and then the electrons will transfer

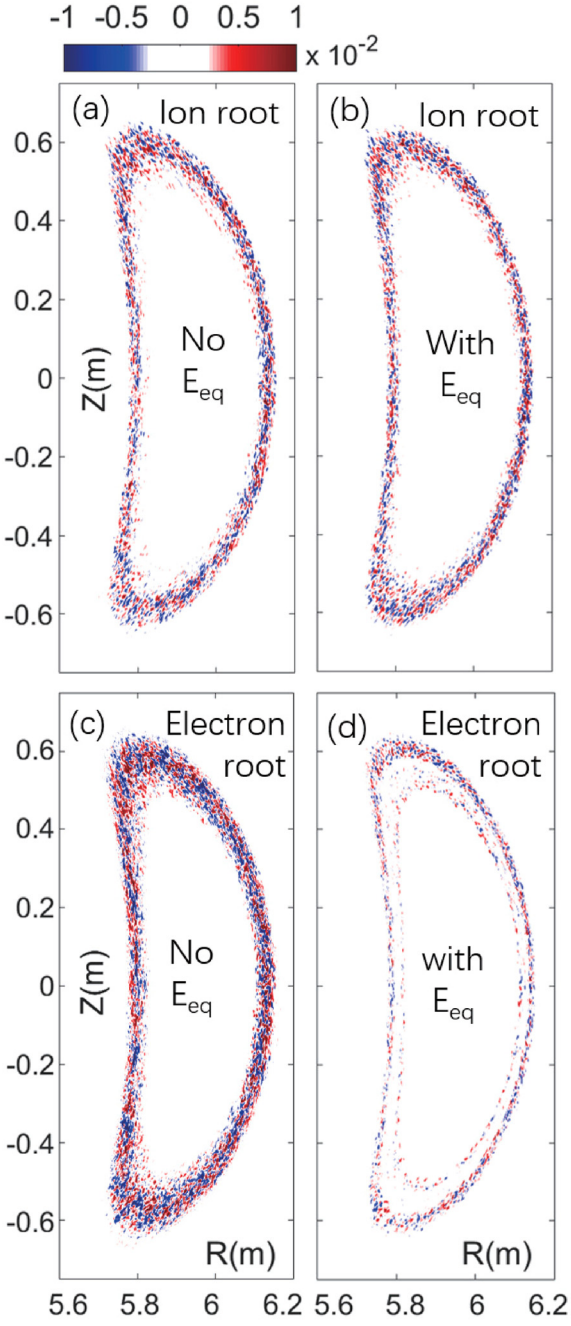

FIG. 10. Contour plots of nonzonal potential $e\delta\phi/T_e$ on the $\zeta = 0$ poloidal plane after ITG saturation in ion root case at $t = 25R_0/C_s$ [panels (a) and (b)] and in the electron root case at $t = 80R_0/C_s$ [panels (c) and (d)] with or without E_{eq}.

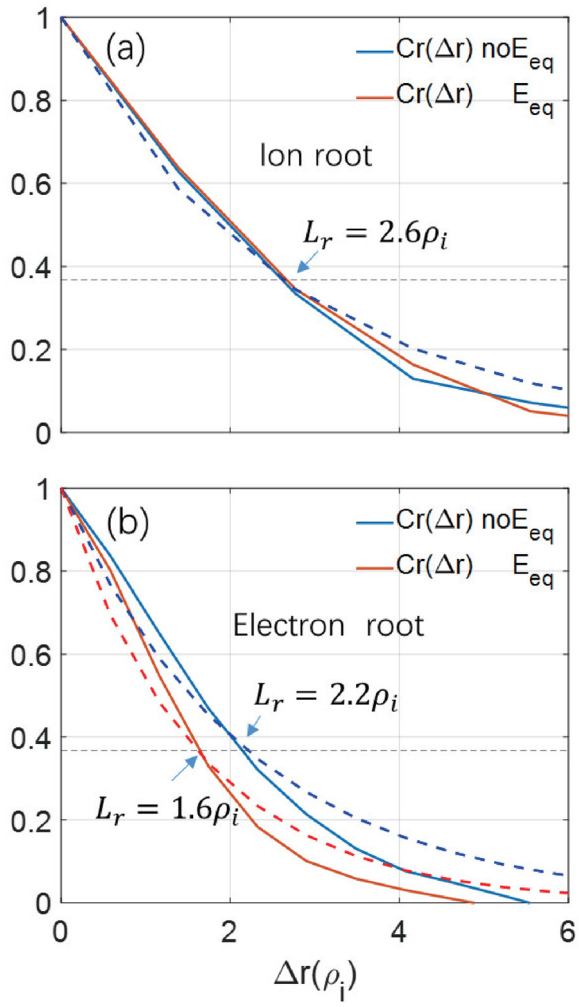

FIG. 11. Time-averaged radial correlation function C_r vs radial separation Δr for nonzonal potential after ITG saturation from simulations with or without ambipolar electric field E_{eq} in ion root case [panel (a)] and electron root case [panel (b)]. The C_r is fitted with an exponential decay (dashed lines).

their energy to the thermal ions resulting in an electron temperature higher than the ion temperature.

In future turbulence simulations, we will include the effects of kinetic electrons (especially roles of helically trapped electrons in the stellarator), which could enhance ITG instability and excited new trapped electron mode. We will also develop coupled neoclassical and turbulence simulations, where both neoclassical transport and turbulence transport are treated on the same footing. On one hand, neoclassical transport (including ambipolar electric field) could be affected by the microturbulence acting as an effective collision in the particle phase space.[52] On the other hand, Coulomb collisions could damp zonal flows that regulate the microturbulence,[53] and neoclassical simulation is needed to provide an accurate equilibrium distribution function for the turbulence simulation.

ACKNOWLEDGMENTS

The W7-X model equilibrium used in this work was originally generated by Dr. Joachim Geiger and published in Refs. 13 and 21. The authors would like to thank J. Riemann, R. Kleiber, D. A. Spong, and H. Y. Wang for providing the W7-X equilibrium data

and for useful discussions. We acknowledge technical support by the GTC team. This work was supported by the China National Magnetic Confinement Fusion Science Program (Grant Nos. 2017YFE0301300 and 2018YFE0304100); the U.S. Department of Energy, Office of Science, Office of Advanced Scientific Computing Research and Office of Fusion Energy Sciences, Scientific Discovery through Advanced Computing (SciDAC) program under Award Nos. DE-SC0018270 and DE-SC0020413 (SciDAC ISEP Center). This work used the resources of the Oak Ridge Leadership Computing Facility at the Oak Ridge National Laboratory (DOE Contract No. DE-AC05-00OR22725) and the National Energy Research Scientific Computing Center (DOE Contract No. DE-AC02-05CH11231).

DATA AVAILABILITY

The data that support the findings of this study are available from the corresponding author upon reasonable request.

REFERENCES

[1]L. Spitzer, Jr., Phys. Fluids **1**, 253 (1958).
[2]V. D. Shafranov, Nucl. Fusion **20**, 1075 (1980).
[3]A. H. Boozer, Nucl. Fusion **55**, 025001 (2015).
[4]A. Dinklage, C. D. Beidler, P. Helander, G. Fuchert, H. Maaßberg, K. Rahbarnia, T. Sunn Pedersen, Y. Turkin, R. C. Wolf, A. Alonso *et al.*, Nat. Phys. **14**, 855 (2018).
[5]N. A. Pablant, A. Langenberg, A. Alonso, C. D. Beidler, M. Bitter, S. Bozhenkov, R. Burhenn, M. Beurskens, L. Delgado-Aparicio, A. Dinklage *et al.*, Phys. Plasmas **25**, 022508 (2018).
[6]E. M. Edlund, M. Porkolab, Z. Huang, O. Grulke, L. G. Böttger, C. von Sehren, and A. von Stechow, Rev. Sci. Instrum. **89**, 10E105 (2018).
[7]H. E. Mynick and W. N. G. Hitchon, Nucl. Fusion **23**, 1053 (1983).
[8]T. S. Hahm and K. H. Burrell, Phys. Plasmas **2**, 1648 (1995).
[9]K. Itoh, S. Toda, A. Fujisawa, S.-I. Itoh, M. Yagi, A. Fukuyama, P. H. Diamond, and K. Ida, Phys. Plasmas **14**, 020702 (2007).
[10]U. Stroth, K. Itoh, S.-I. Itoh, H. Hartfuss, H. Laqua, ECRH Team, and W7-AS Team, Phys. Rev. Lett. **86**, 5910 (2001).
[11]T. Minami, A. Fujisawa, H. Iguchi, Y. Liang, K. Ida, S. Nishimura, M. Yokoyama, S. Murakami, Y. Yoshimura, and M. Isobe, Nucl. Fusion **44**, 342 (2004).
[12]K. Ida, T. Shimozuma, H. Funaba, K. Narihara, S. Kubo, S. Murakami, A. Wakasa, M. Yokoyama, Y. Takeiri, K. Y. Watanabe *et al.*, Phys. Rev. Lett. **91**, 085003 (2003).
[13]J. Riemann, R. Kleiber, and M. Borchardt, Plasma Phys. Controlled Fusion **58**, 074001 (2016).
[14]P. Xanthopoulos, S. A. Bozhenkov, M. N. Beurskens, H. M. Smith, G. G. Plunk, P. Helander, C. D. Beidler, J. A. Alcusón, A. Alonso, A. Dinklage *et al.*, Phys. Rev. Lett. **125**, 075001 (2020).
[15]H. Biglari and P. H. Diamond, Phys. Fluids B: Plasma Phys. **2**, 1 (1990).
[16]T.-H. Watanabe, H. Sugama, and S. Ferrando-Margalet, Nucl. Fusion **47**, 1383 (2007).
[17]P. Xanthopoulos, F. Merz, T. Gorler, and F. Jenko, Phys. Rev. Lett. **99**, 035002 (2007).
[18]B. J. Faber, M. J. Pueschel, P. W. Terry, C. C. Hegna, and J. E. Roman, J. Plasma Phys. **84**(5), 905840503 (2018).
[19]M. A. Beer, S. C. Cowley, and G. W. Hammett, Phys. Plasmas **2**, 2687 (1995).
[20]J. W. Connor, R. J. Hastie, and J. B. Taylor, Phys. Rev. Lett. **40**, 6 (1978).
[21]H. Y. Wang, I. Holod, Z. Lin, J. Bao, J. Y. Fu, P. F. Liu, J. H. Nicolau, D. Spong, and Y. Xiao, Phys. Plasmas **27**, 082305 (2020).
[22]M. D. J. Cole, T. Moritaka, R. Hager, J. Dominski, S. Ku, and C. S. Chang, Phys. Plasmas **27**, 044501 (2020).
[23]A. Bañon Navarro, G. Merlo, G. G. Plunk, P. Xanthopoulos, A. von Stechow, A. Di Siena, M. Maurer, F. Hindenlang, F. Wilms, and F. Jenko, Plasma Phys. Controlled Fusion **62**, 105005 (2020).
[24]J. Smoniewski1, E. Sánchez, I. Calvo, M. J. Pueschel, and J. N. Talmadge, Phys. Plasmas **28**, 042503 (2021).
[25]Z. Lin, W. M. Tang, and W. W. Lee, Phys. Plasmas **2**, 2975 (1995).
[26]Z. Lin, T. S. Hahm, W. W. Lee, W. M. Tang, and R. B. White, Science **281**, 1835 (1998).
[27]A. Reiman, G. Fu, S. Hirshman, L. Ku, D. Monticello, H. Mynick, M. Redi, D. Spong, M. Zarnstorff, and B. Blackwell, Plasma Phys. Controlled Fusion **41**, B273 (1999).
[28]J. L. V. Lewandowski, J. Williams, A. H. Boozer, and Z. Lin, Phys. Plasmas **8**, 2849 (2001).
[29]J. Y. Fu, P. F. Liu, X. S. Wei, Z. Lin, Z. Lin, N. Ferraro, and R. Nazikian, "Effect of Resonant Magnetic Perturbations on Radial Electric fields in DIII-D Tokamak" (unpublished).
[30]I. Holod, Z. Lin, S. Taimourzadeh, R. Nazikian, D. Spong, and A. Wingen, Nucl. Fusion **57**, 016005 (2017).
[31]G. Dong and Z. Lin, Nucl. Fusion **57**, 036009 (2017).
[32]K. S. Fang and Z. Lin, Phys. Plasmas **26**, 052510 (2019).
[33]P. Helander, Rep. Prog. Phys. **77**, 087001 (2014).
[34]A. J. Brizard and T. S. Hahm, Rev. Mod. Phys. **79**, 2 (2007).
[35]W. W. Lee, Phys. Fluids **26**, 556 (1983).
[36]S. E. Parker and W. W. Lee, Phys. Fluids B: Plasma Phys. **5**, 77 (1993).
[37]G. Hu and J. A. Krommes, Phys. Plasmas **1**, 4 (1994).
[38]W. X. Wang, F. L. Hinton, and S. K. Wong, Phys. Rev. Lett. **87**, 055002 (2001).
[39]R. B. White and M. S. Chance, Phys. Fluids **27**, 10 (1984).
[40]S. P. Hirshman and J. C. Whitson, Phys. Fluids **26**, 12 (1983).
[41]A. H. Boozer, Phys. Fluids **24**, 1999 (1981).
[42]Y. Xiao, I. Holod, Z. Wang, Z. Lin, and T. Zhang, Phys. Plasmas **22**, 022516 (2015).
[43]N. A. Pablant, A. Langenberg, A. Alonso, C. D. Beidler, M. Bitter, S. Bozhenkov, R. Burhenn, M. Beurskens, L. Delgado-Aparicio, A. Dinklage *et al.*, Nucl. Fusion **57**, 102020 (2017).
[44]P. Helander, A. Mishchenko, R. Kleiber, and P. Xanthopoulos, Plasma Phys. Controlled Fusion **53**, 054006 (2011).
[45]D. D.-M. Ho and R. M. Kulsrud, Phys. Fluids **30**, 442 (1987).
[46]L. M. Kovrizhnykh, Nucl. Fusion **24**, 851 (1984).
[47]Z. Lin and T. S. Hahm, Phys. Plasmas **11**, 3 (2004).
[48]I. Holod and Z. Lin, Phys. Plasmas **14**, 032306 (2007).
[49]T. H. Watanabe, H. Sugama, and M. Nunami, Nucl. Fusion **51**, 123003 (2011).
[50]U. Losada, A. Alonso, B. Ph. van Milligen, C. Hidalgo, B. Liu, M. A. Pedrosa, C. Silva, and TJ-II Team, Plasma Phys. Controlled Fusion **58**, 084005 (2016).
[51]Z. Lin, I. Holod, L. Chen, P. H. Diamond, T. S. Hahm, and S. Ethier, Phys. Rev. Lett. **99**, 265003 (2007).
[52]H. E. Mynick and A. H. Boozer, Phys. Plasmas **12**, 062513 (2005).
[53]Z. Lin, T. S. Hahm, W. W. Lee, W. M. Tang, and P. H. Diamond, Phys. Rev. Lett. **83**, 3645 (1999).